Journal for ImmunoTherapy of Cancer

# First-in-human single-cell and TCR atlas reveals peripheral immune remodeling before and after irreversible electroporation in prostate cancer

Jia-Cheng Xiang, Zhi-Yu Xia, Jian-Xuan Sun, Gui-Chen Ye, Yuan Wang, Jun Yang, Shao-Gang Wang , Qi-Dong Xia

**To cite:** Xiang J-C, Xia Z-Y, Sun J-X, *et al*. First-in-human single-cell and TCR atlas reveals peripheral immune remodeling before and after irreversible electroporation in prostate cancer. *Journal for ImmunoTherapy of Cancer* 2026;**14**:e014288. doi:10.1136/jitc-2025-014288

► Additional supplemental material is published online only. To view, please visit the journal online (https://doi.org/10.1136/jitc-2025-014288).

JY, S-GW and Q-DX contributed equally.
J-CX and Z-YX contributed equally.

J-CX and Z-YX are joint first authors.

Accepted 13 April 2026



Department of Urology, Huazhong University of Science and Technology Tongji Medical College Tongji Hospital, Wuhan, Hubei, China

**Correspondence to**
Dr Qi-Dong Xia;
qidongxia_md@163.com

Professor Shao-Gang Wang;
sgwangtjm@163.com

Professor Jun Yang;
jyang0105@hust.edu.cn

## ABSTRACT

**Background** Prostate cancer (PCa) is the second most common malignancy in men worldwide. Although radical prostatectomy effectively controls tumor progression, it often causes complications such as urinary incontinence and sexual dysfunction. Irreversible electroporation (IRE), a non-thermal ablation technique that preserves neurovascular structures, has emerged as a promising focal therapy and may induce systemic antitumor immunity through immunogenic cell death. However, the mechanisms and temporal dynamics of systemic immune responses to IRE in humans remain unclear.

**Methods** This prospective study enrolled five patients with localized PCa (T2a–T2c). Peripheral blood samples were collected before and 7 days after IRE treatment. Single-cell RNA sequencing and T-cell receptor (TCR) repertoire profiling (10x Genomics) were performed to construct a high-resolution immune landscape. Integrated bioinformatic analyses—including Seurat/Harmony clustering, differential expression, functional enrichment, Gene Set Variation Analysis, transcription factor analysis, cell–cell communication (CellChat), and clonal tracking (Immunarch/scRepertoire)—were used to characterize systemic immune modulation following IRE.

**Results** IRE induced bidirectional remodeling of the peripheral immune landscape. Myeloid cells, especially non-classical monocytes, increased in proportion and exhibited activation of inflammatory (interleukin-27), antiviral, complement, and antigen presentation pathways. T cells declined and exhibited reduced activation-associated and proliferation-associated transcriptional programs alongside enhanced survival-related signaling, consistent with a relative quiescent state of peripheral adaptive immunity at day 7. Natural killer cells showed elevated cytotoxic activity. TCR profiling revealed increased diversity and antigen-driven clonal expansion, while cell–cell communication shifted toward proinflammatory (TNF/SELPLG) and away from antigen-presenting (major histocompatibility complex (MHC)-I/CD40) interactions, indicating coordinated innate-adaptive rebalancing.

**Conclusion** This study is the first to map systemic immune dynamics after IRE in prostate cancer using single-cell analysis. 1 week after IRE, peripheral blood mononuclear cells show robust innate activation with concomitant attenuation of circulating T-cell activation/proliferation and reduced MHC-I/CD40-related communication, consistent with a time-dependent systemic immune rebalancing phase rather than sustained peak adaptive activation in blood. These findings support time-resolved immune monitoring and may help optimize the timing of IRE-based combination immunotherapy.

### WHAT IS ALREADY KNOWN ON THIS TOPIC

⇒ Irreversible electroporation (IRE) is an organ-preserving focal therapy for localized prostate cancer and has been proposed to induce antitumor immune responses. However, high-resolution evidence defining systemic immune remodeling after IRE in human prostate cancer has remained limited, particularly at the single-cell and T-cell receptor (TCR) repertoire levels.

### WHAT THIS STUDY ADDS

⇒ Using paired pre-IRE and post-IRE peripheral blood mononuclear cell single-cell RNA sequencing and TCR profiling, this study provides a first-in-human atlas of peripheral immune remodeling after IRE in localized prostate cancer. We show that postoperative day 7 is characterized by strong innate immune activation, relative attenuation/rebalancing of circulating adaptive immune programs, selective TCR clonal remodeling, and subset-specific checkpoint receptor/ligand changes in T/natural killer and myeloid compartments.

### HOW THIS STUDY MIGHT AFFECT RESEARCH, PRACTICE OR POLICY

⇒ These findings support time-resolved immune monitoring after IRE and provide a rationale for optimizing the timing of combination strategies with immunotherapy, including checkpoint blockade. More broadly, this work offers a clinically relevant reference resource for future translational studies of focal therapy-induced immune remodeling in prostate cancer.

## INTRODUCTION

Prostate cancer (PCa) remains a formidable global health challenge, ranking as the second most common malignancy and a leading cause of cancer-related mortality in

men.[1 2] The clinical management of localized PCa presents a complex landscape, encompassing a spectrum of options from watchful waiting/active surveillance for low-risk lesions to radical interventions such as prostatectomy and radiotherapy for higher-risk cases.[3] While these conventional treatments offer high rates of oncological control, they are frequently associated with significant morbidity, including urinary incontinence, erectile dysfunction, and bowel-related complications, which can profoundly impair a patient's quality of life. This therapeutic dilemma has catalyzed the development of minimally invasive, focal therapies aimed at achieving effective cancer ablation while preserving surrounding critical structures and minimizing functional sequelae.[4–6] Among these emerging modalities, irreversible electroporation (IRE) has garnered considerable attention as a novel, non-thermal ablation technique.

IRE uses the delivery of high-frequency, high-voltage electrical pulses (1,000–2,000 V/cm) across targeted tissue. These pulses induce the formation of nanoscale defects, or pores, in the cell membrane lipid bilayer. When the electrical field strength surpasses a critical threshold, the resulting poration transitions to irreversibility, triggering disruption of cellular homeostasis and ultimately inducing apoptosis.[7 8] The cardinal advantage of IRE lies in its purported non-thermal mechanism and its ability to selectively spare proteins and the extracellular matrix. This selectivity allows for the precise ablation of target tissue while preserving vital adjacent structures such as blood vessels, nerves, and urinary sphincters, a feature that positions IRE as a particularly attractive option for the treatment of PCa lesions in close proximity to neurovascular bundles or the prostatic urethra.[9]

Beyond its direct cytotoxic effects, a growing body of preclinical evidence suggests that IRE may possess significant immunomodulatory potential. The premise is that IRE, by inducing immunogenic cell death, can transform the immunosuppressive tumor microenvironment (TME) into a pro-inflammatory state conducive to the initiation of a systemic antitumor immune response.[8 10] Apoptosis, as the primary mode of IRE-induced cell death, is traditionally considered immunologically silent or tolerogenic.[11] However, the unique nature of IRE—a physical disruption that may allow the release of tumor-associated antigens (TAAs) and damage-associated molecular patterns (DAMPs) in a controlled, non-necrotic manner—could potentially break this paradigm. Theoretically, this "in situ vaccination" effect could lead to the uptake of TAAs by antigen-presenting cells, such as dendritic cells (DCs), their subsequent migration to draining lymph nodes, and the priming and activation of tumor-specific T cells.[12] This cascade could not only target residual local disease but also elicit a systemic effect against potential micrometastases, a concept known as the abscopal effect.[13] Despite this compelling hypothesis, high-resolution evidence characterizing the systemic immune response to IRE in human patients with PCa remains limited. Notably, a recent prospective study (IRE-IMMUNO) reported multi-time point peripheral immune changes after IRE in localized PCa using flow cytometry and enzyme-linked immunospot (ELISpot), including reduced immune suppression and delayed effector T-cell activation; however, single-cell and clonotype-resolved characterization of early post-IRE immune remodeling remains insufficiently defined.[14]

The advent of high-throughput single-cell RNA sequencing (scRNA-seq) has revolutionized our capacity to deconvolute the intricate cellular heterogeneity of the immune system.[15] Unlike bulk RNA sequencing, which provides an averaged transcriptomic profile, scRNA-seq enables the unbiased identification and characterization of rare and novel cell subpopulations, the delineation of cellular developmental trajectories, and the analysis of cell–cell communication networks at an unprecedented resolution. In the context of cancer immunotherapy, scRNA-seq has been instrumental in identifying predictive biomarkers of response, mechanisms of resistance, and the dynamic shifts in immune cell composition and state following therapeutic intervention.[16] Applying this powerful technology to the peripheral blood of patients with cancer offers a unique window into the systemic immune landscape, allowing for the monitoring of immune cell mobilization, activation, and exhaustion in response to localized treatments like IRE.

To address the critical knowledge gap regarding IRE's systemic immunologic impact in human PCa, we designed a prospective paired pretreatment and post-treatment study. We hypothesized that focal IRE induces measurable remodeling of the peripheral immune repertoire. We selected postoperative day 7 as a biologically informed early time point to capture early systemic immune changes following IRE, rather than to define the peak response. Although day 7 is biologically relevant for early immune changes, the kinetics of post-IRE immune responses in humans remain uncertain; therefore, this time point may reflect ongoing immune priming in some compartments and/or an early transition toward immune rebalancing in the peripheral circulation. To test this, we performed comprehensive scRNA-seq, coupled with T-cell receptor (TCR) sequencing, on peripheral blood mononuclear cells (PBMCs) collected from five patients with localized PCa at two critical time points: preoperatively (baseline) and at a standardized postoperative time point of 7 days. This design allows for each patient to serve as their own control, enabling a precise dissection of immune alterations directly attributable to the IRE procedure.

In this paper, we present a detailed analysis of paired single-cell data collected before and after IRE. Our primary objective is to identify and quantify the specific alterations in immune cell subsets, their transcriptional states, and TCR clonality induced by IRE treatment in the postoperative phase. The findings from this investigation aim to provide the first high-resolution atlas of the systemic immune response to IRE in human PCa, shedding light on its underlying mechanisms and potentially informing future strategies to combine IRE with immunotherapeutic agents to enhance treatment efficacy.

## METHODS

### Research design and patient recruitment

The study aimed to reveal changes in the peripheral blood single-cell landscape of patients with PCa following IRE therapy. A total of five patients were enrolled, all meeting our predefined inclusion criteria: (1) localized tumor without pelvic lymph node or distant metastasis; (2) confirmed PCa by core needle biopsy; (3) tumor maximum diameter ≤3.0 cm confirmed by ultrasound, CT, and MRI; (4) male patients aged ≥18 years without coagulation disorders, chronic liver disease, renal failure, immune system disorders, infectious diseases, or other acute/chronic conditions potentially affecting immune response. All enrolled patients provided informed consent. All experiments were conducted in compliance with the Declaration of Helsinki.

### The IRE treatment process

IRE for PCa was performed using the G1 Composite Steep Pulse Therapy Device (Shanghai Ruidao Medical). Under transrectal ultrasound guidance (BK Flex Focus 500), disposable electrodes were perineally inserted in parallel into the target lesion (tip exposure 5–40 mm; spacing 0.5–2 cm). Pulse parameters were set to 500–3,000 V (field strength 1,000–1,500 V/cm) with microsecond pulse durations and a 1 Hz burst frequency. Bipolar high-voltage pulses were sequentially delivered for complete tumor ablation. Post-procedure, treatment reports were generated, and patients were monitored for adverse events. Detailed surgery information for each patient was demonstrated in online supplemental Table S1.

### Sample collection and PBMCs isolation

In this pilot study, postoperative day 7 was prespecified as a standardized early sampling time point to assess systemic immune remodeling after IRE; additional interim postoperative blood draws were not available. Peripheral blood (5 mL) was collected from patients 1 day before and 7 days after IRE treatment using EDTA tubes. Samples were diluted 1:1 with phosphate-buffered saline (PBS) and layered onto Ficoll lymphocyte separation medium (Solarbio, P4350) for density gradient centrifugation. The PBMC layer was harvested, washed two times with PBS, and resuspended in Roswell Park Memorial Institute (RPMI) 1640 medium containing 0.04% bovine serum albumin (BSA). Cells were stored at −80°C until further processing.

### Single-cell RNA sequencing of PBMCs

Single-cell suspensions (700–1,200 cells/μL) were mixed with Master Mix and loaded onto a Chromium Chip B (10x Genomics) for GEM generation on the Chromium Controller. Reverse transcription was performed to produce complementary DNA (cDNA), which was then purified with DynaBeads Silane and amplified by PCR to construct cDNA libraries. After purification with SPRIselect beads, 10 μL of amplified cDNA was fragmented, end-repaired, and adaptor-ligated. Indexed libraries were generated through PCR amplification and dual-step SPRIselect purification. Library quality was assessed using Qubit and Agilent Bioanalyzer (400–600 bp), and qualified libraries were sequenced (PE150) on the Illumina NovaSeq 6000 platform.

### TCR immunorepertoire sequencing for PBMC

Single-cell suspensions (700–1,200 cells/μL in RPMI 1640 with 0.04% BSA) were processed on the 10x Genomics Chromium platform (Next GEM Single Cell 5' Kit V.2) to generate GEM droplets for reverse transcription and cDNA amplification. T-cell receptor V(D)J regions were enriched using the Chromium Single Cell V(D)J Enrichment Kit (Human T Cell) and amplified with the corresponding TCR Amplification Kit. After quality control, libraries were sequenced on the Illumina NovaSeq 6000 platform (PE150), yielding approximately 10 Gb per sample.

### Upstream analysis of raw data and quality control

Raw sequencing data were aligned to the human reference genome (GRCh38) using Cell Ranger (V.9.0.0) to generate feature-barcode matrices. Quality control was conducted in Seurat (V.4.4.0).[17] Doublets were identified and removed using DoubletFinder (V.2.0.3) with an estimated doublet rate of 0.8%. High-quality cells were defined by 200–5,000 detected genes, 500–7,500 unique molecular identifiers (UMIs), <10% mitochondrial, and <5% hemoglobin gene content. Ambiguous subpopulations (6,677 cells) were excluded. After rigorous filtering, 171,977 cells were retained for downstream analysis, with a median of 1,469 genes and 3,021 UMIs per cell.

### Standardized data processing and dimensionality reduction clustering

To remove batch effects and delineate intrinsic cell structures, quality-controlled data were normalized, log-transformed, and scaled after selecting 2,000 highly variable genes. Principal component analysis was applied for linear dimensionality reduction, followed by batch correction using the Harmony algorithm with sample origin as the covariate. The integrated embeddings (first 20 dimensions) were visualized by Uniform Manifold Approximation and Projection (UMAP), and unsupervised clustering was performed using the graph-based Louvain method (resolution=0.6). Batch correction efficiency and clustering accuracy were verified by comparing sample distributions before and after integration. For global visualization and cell-type annotation, we integrated cells across all samples using Harmony. Pooled, integrated data were used for descriptive analyses and gene-program discovery, whereas key conclusions were cross-checked using paired within-patient (post vs pre) comparisons to account for inter-individual variability.

### Identification of marker genes and annotation of cell types

Marker gene identification was achieved through differential expression analysis: the FindAllMarkers function (Presto algorithm) in Seurat (V.4.4.0) evaluated genes upregulated in each cell cluster relative to the others to screen candidate markers. To define each subpopulation, we annotated single-cell transcriptomic data using scMayoMap and[18 19] ACT database. By integrating outcomes from both methods and visualizing them alongside known biological knowledge and literature-reported markers for each subpopulation, we ultimately confirmed the type annotations for each cell subpopulation and used dot plot to visualize the expression of specific cell markers across different subpopulations. Due to the transcriptional similarity between T and natural killer (NK) cells, we first annotated them at the lineage level as a combined T/NK compartment and then performed dedicated subclustering to resolve finer T-cell and NK-cell subsets.

### Differential analysis and functional enrichment

Differentially expressed genes (DEGs) were identified using the FindMarkers function in Seurat (V.4.4.0) with the "presto" test. Genes with Bonferroni-adjusted $p<0.05$ and $|\log_2 \text{foldchange}|>0.26$ were considered significant. Functional enrichment of DEGs was analyzed using hypergeometric tests based on Kyoto Encyclopedia of Genes and Genomes (KEGG) and Gene Ontology (GO) databases to determine associated biological processes, molecular functions, and signaling pathways ($p<0.05$).

### GSVA enrichment analysis

Gene Set Variation Analysis (GSVA) was conducted using the GSVA (V.1.30.0) and GSEABase (V.1.44.0) packages with predefined KEGG and GO gene sets.[20] Normalized expression data were transformed into pathway activity scores for each cell using a non-parametric kernel estimation algorithm. Differential pathway activities between clusters or groups were assessed with the LIMMA package (V.3.38.3), and pathways with $p<0.05$ were considered significantly enriched or suppressed. Pathway-level comparisons were performed at the cohort level (post vs pre) to identify shared trends, and patient-wise analyses were additionally used to confirm the directionality of key pathway changes across individuals. For GO terms containing "positive regulation" or "negative regulation," pathway direction was reported as the change in enrichment score of the annotated term itself, and biological interpretation was made conservatively without assuming the net downstream functional effect from the term title alone.

### Immune repertoire analysis

TCR data from PBMCs were analyzed using Immunarch (V.0.6.8) and scRepertoire (V.v1.9.1). TRA/TRB paired sequences were integrated and annotated by treatment group (pre-IRE, post-IRE). Clonal abundance, CDR3 length, V(D)J gene usage, and diversity indices (Shannon, Simpson) were calculated to assess clonal expansion and diversity. Clonal overlap and β-chain CDR3 motif analyses characterized sequence convergence. Integrated TCR and transcriptomic data (via combineExpression()) enabled visualization of clonal size and expansion patterns in UMAP space, revealing dynamic T-cell clonal remodeling before and after IRE. Repertoire metrics were summarized at the cohort level and further examined in a patient-wise manner (eg, top clonotype fractions) to ensure that patterns were not driven by a single individual.

### Cell chat analysis

Cell–cell communication was analyzed using the CellChat R package (V.2.1.2) to infer ligand-receptor signaling networks. The standardized single-cell matrix was processed to identify overexpressed genes and interactions, followed by calculation of communication probabilities and filtering of low-frequency pairs (min. cells=10). Interaction probabilities were integrated into pathway hierarchies and aggregated into inter-cluster networks. Visualization with ggalluvial highlighted dominant signaling pathways and key regulatory interactions.

### Transcription factor prediction analysis

Transcription factor (TF) regulatory networks were inferred using the SCENIC workflow (V.1.2.4).[21] Gene co-expression modules were first constructed with GRNboost, and enriched TF-target regulons were identified through motif analysis in RcisTarget (Normalized Enrichment Score (NES) >3.0, area under the curve (AUC) >0.05). Regulon activity scores were quantified for each cell using AUCell, and regulatory specificity was evaluated via Regulatory Specificity Scores (RSS) and Correlation Strength Index to identify key cell type-specific TFs.

## RESULTS

### Study design and patients characteristics

This study aims to investigate changes in the PBMC landscape of patients with PCa undergoing IRE treatment using single-cell sequencing, thereby analyzing the therapeutic immune response to IRE (figure 1A). The study protocol is provided in the supplemental materials (see online supplemental Materials). A total of five patients were enrolled, ranging in age from 58 to 82 years old. Tumor T-stages ranged from T2a to T2c. Pretreatment prostate-specific antigen (PSA) concentrations varied from 4.63 to 14.69 ng/mL across all patients. Post-treatment, PSA levels significantly decreased in all patients, ranging from 0.31 to 0.64 ng/mL. For each patient, we also collected data on Gleason score, ISUP grade, surgical timing, and specific surgical procedures. Detailed patient

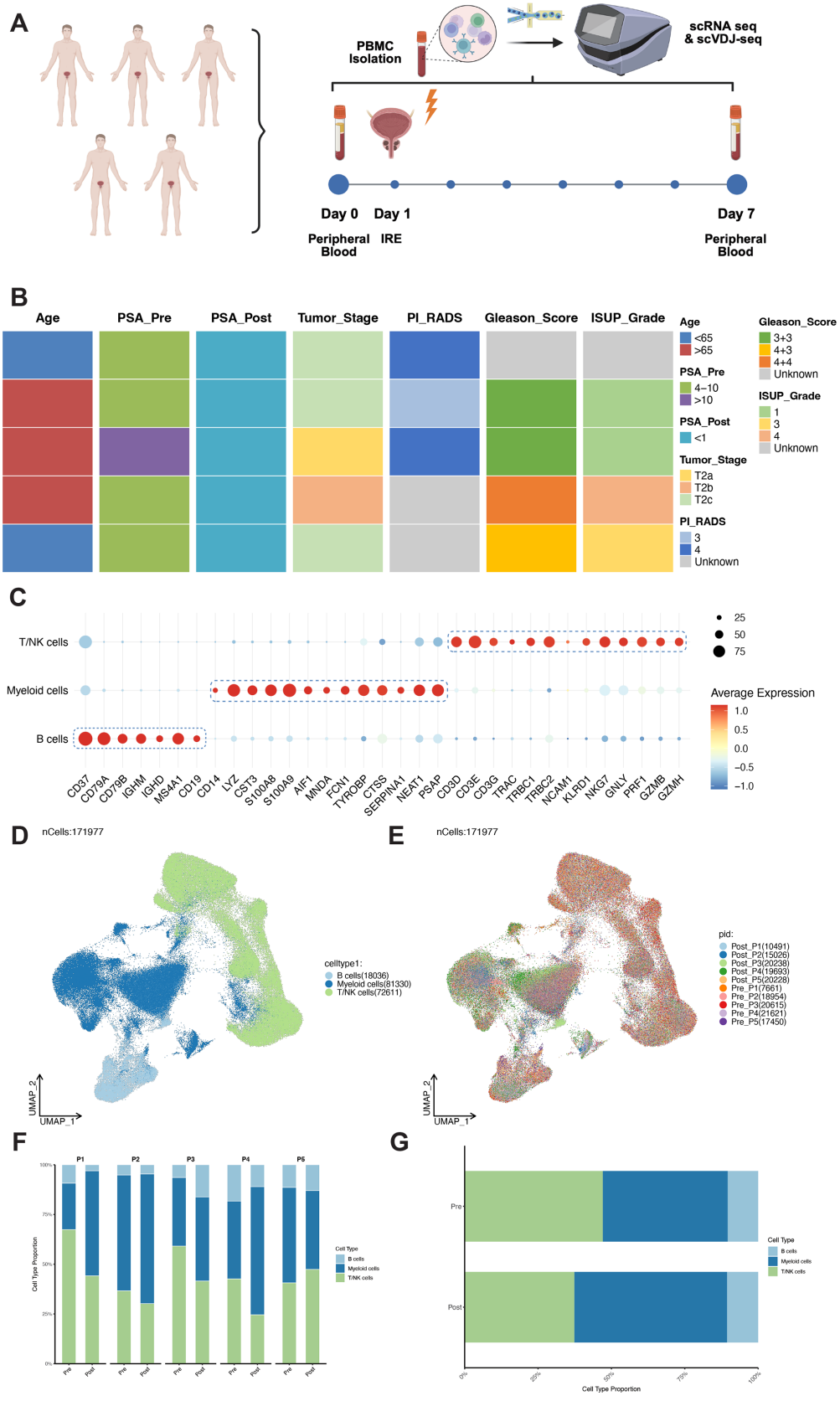


**Figure 1** (A) Study design of our research. (B) Clinical information of the patients. (C) The expression of specific markers by T/NK cells, myeloid cells and B cells. (D) The UMAP dimension reduction of T/NK cells, myeloid cells and B cells. (E) The dimensionality reduction of UMAP in cells from each patient. (F) The proportions of T/NK cells, myeloid cells and B cells among the five patients. (G) The overall proportion of T/NK cells, myeloid cells and B cells. IRE, irreversible electroporation; NK, natural killer; PBMC, peripheral blood mononuclear cell; PSA, prostate-specific antigen; scRNA-seq, single-cell RNA sequencing; UMAP, Uniform Manifold Approximation and Projection.

information is summarized in online supplemental Table S1 and figure 1B.

After excluding low-quality cells through standardized quality control (online supplemental Figure S1), we ultimately included 171,977 cells for subsequent analysis. We analyzed the expression of representative markers for classical PBMC cell populations, ultimately identifying 72,611 T/NK cells, 81,330 myeloid cells, and 18,036 B cells (figure 1C–E). In T/NK cells, characteristic genes such as CD3D, TRAC, NCAM1, KLRD1, NKG7, GNLY, PRF1, and GZMB were significantly overexpressed. Similarly, myeloid cells showed significantly elevated expression of genes including CD14, LYZ, CST3, S100A8, CTSS, and SERPINA1, while B cells exhibited markedly higher expression of characteristic genes such as CD37, CD79A, CD79B, IGHM, IGHD, MS4A1, and CD19. In terms of cellular proportions before and after treatment, the overall myeloid cell proportion increased following IRE therapy (elevated in four patients, with a slight decrease in P5), while the T/NK cell proportion decreased (decreased in four patients, with a slight increase in P5). B cells showed no significant fluctuation (figure 1F,G). Throughout the study, cohort-level summaries are presented to highlight shared patterns, while patient-wise paired comparisons are provided (main figures and online supplemental figure) to demonstrate consistency and interpatient heterogeneity.

### Overall functional transformation of PBMCs following IRE treatment

Following IRE treatment, multiple pathways associated with inflammation and immune activation were upregulated in patients with PCa's PBMCs. These primarily included pyrogenic production, complement activation, leukocyte and macrophage activation, interleukin (IL)-27-mediated signaling, autocrine regulation, antivirus response and adhesion molecule production (figure 2A). This upregulation predominantly occurs in myeloid cells, suggesting that IRE induces myeloid cell-mediated inflammatory responses and innate immune activation, thereby promoting antitumor immune responses (figure 2B–D). However, functional activities associated with T cells and NK cells in PBMCs exhibited a relatively quiescent and suppressed state. Downregulated pathways included $CD4^+$/$CD8^+$ T-cell proliferation and differentiation, T-cell activation and apoptosis regulation, and NK/T-cell differentiation, suggesting a temporary reduction in adaptive immune cell activity following IRE treatment (figure 2E). This downregulation primarily occurred within T/NK cells (figure 2F–H). Conclusively, inflammatory pathways associated with myeloid cells and innate immune pathways were significantly upregulated, while proliferation and differentiation pathways related to T/NK cells were downregulated. These findings suggest that, at the postoperative day 7 peripheral blood time point, IRE is associated with prominent innate immune activation, whereas circulating adaptive immune programs are in a relatively quiescent/rebalancing state.

### Distinct transcriptomic reprogramming of T cells and NK cells at day 7 after IRE

Among 72,611 T/NK cells, CD56dim NK cells (21,362) and $CD4^+$ central memory T cells (22,287) were the most abundant subsets, followed by $CD8^+$ effector memory, γδ T, $CD8^+$ CTL, MAIT, $CD4^+$ CTL, $CD8^+$ naïve, Treg, CD56bright NK, and $CD4^+$ naïve T cells (5,772–830 cells; figure 3A). Proportionally, both CD56dim NK and γδ T cells increased after IRE, whereas regulatory T cell (Treg) cells declined (figure 3B,C). All subsets expressed canonical markers (figure 3D). GO/KEGG enrichment of differentially expressed genes revealed upregulation of immune pathways, including type I interferon-mediated antiviral responses, toll-like and RAGE receptor activity, and NK cell-mediated cytotoxicity (online supplemental Figure S2A,B,D,F and G). Conversely, pathways related to chemokine signaling, cytokine receptor activity, T-cell receptor and NF-κB signaling, adhesion, and differentiation were downregulated (online supplemental Figure S2C,E,G and H). Collectively, these findings indicate that IRE activates antiviral and cytotoxic programs while transiently attenuating T/NK-cell activation, proliferation, and migration.

GSVA analysis across T/NK subtypes confirmed and refined the observed functional alterations (figure 3E–G). IRE induced profound immune reprogramming in T cells, characterized by altered activation states and immune regulatory programs. Upregulated pathways indicated increased tissue migration via integrin biosynthesis and broadened lipid antigen presentation through the major histocompatibility complex (MHC)-Ib pathway (figure 3E). Concurrently, elevated responses to interferon-β and IL-27 promoted a favorable immune milieu, while reduced Treg differentiation alleviated immunosuppression. Downregulation of T-cell and $CD8^+$ T-cell activation and differentiation pathways suggested a transient suppression of effector programs. Both activation-related pathways and pathways annotated as negative regulators of T-cell responses showed reduced GSVA scores after IRE (figure 3F). Taken together, these findings support a relative attenuation and rebalancing of peripheral T-cell functional programs at day 7, rather than sustained proliferative/activation signaling. However, these pathway-level results should be interpreted as transcriptomic signatures and do not by themselves establish specific functional states (figure 3F). Across patients, pathway changes were consistent (online supplemental Figure S3 and S4). Specifically, $CD4^+$ naive T cells showed upregulation of MHC-Ib-mediated lipid antigen presentation and integrin biosynthesis; $CD8^+$ effector memory (EM) T cells upregulated IL-27 and interferon-β responses; and in γδ T cells, $CD8^+$ cytotoxic T lymphocytes (CTLs), and $CD4^+$ CTLs, GSVA scores for GO pathways annotated as negative regulation of $CD8^+$ αβ T-cell activation were decreased (figure 3G, online supplemental Figure S5),

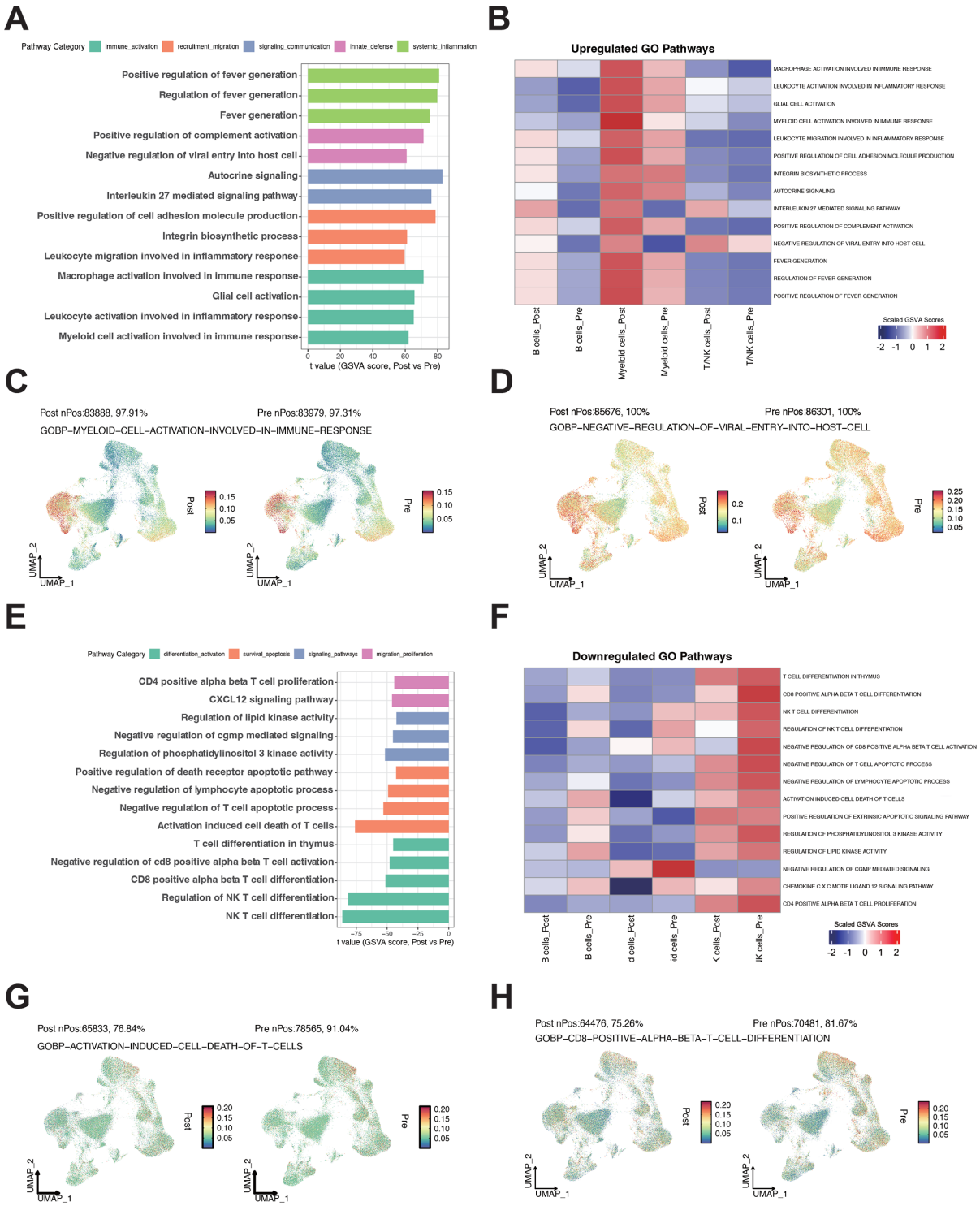


**Figure 2** Significantly upregulated pathways through GSVA analysis (A), as well as the heat maps of the changes in these pathway scores among different cell types (B), and the distribution of key pathways in UMAP dimensionality reduction. (C, D) Significantly downregulated pathways (E), as well as the heat maps of the changes in these pathway scores among different cell types (F), and the distribution of key pathways in UMAP dimensionality reduction (G, H). GO, Gene Ontology; GSVA, Gene Set Variation Analysis; UMAP, Uniform Manifold Approximation and Projection.

indicating reduced enrichment of inhibitory-regulation-related transcriptional programs in these subsets.

In NK cells, multiple innate antiviral and cytokine signaling pathways were significantly upregulated, including IL-27-mediated signaling, interferon-β production, ISG15 conjugation, and MCP-1/IP-10 induction (figure 3H). These changes indicate activation of the interferon axis and enhanced

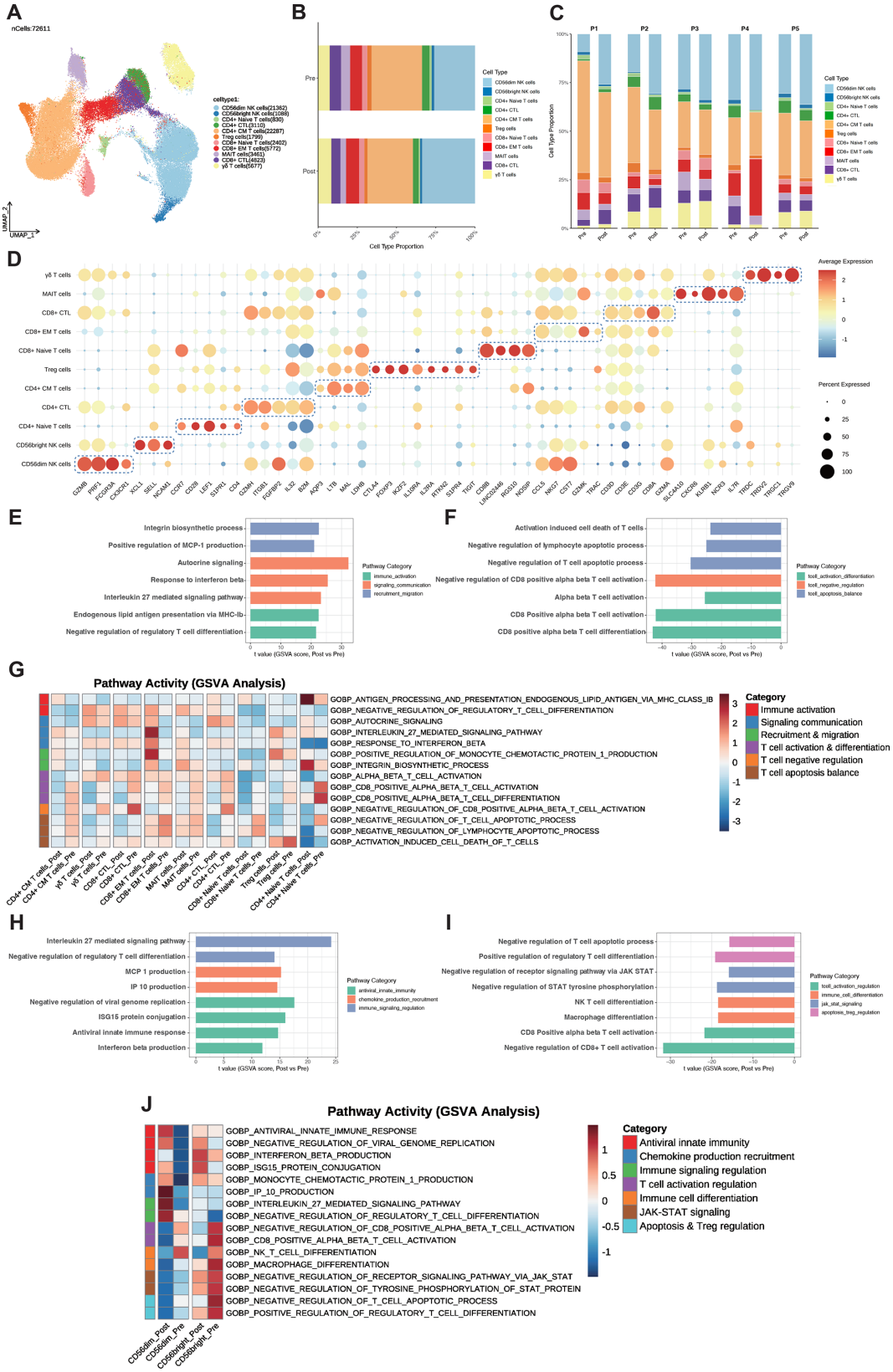


**Figure 3** (A) The UMAP dimensionality reduction results of T/NK cell subtypes. The overall proportion of various T/NK cell subtypes (B) and their proportions in each patient (C). (D) The expression of various T/NK cells for their specific markers. The pathways of significant upregulation (E) and significant downregulation (F) of T cells in GSVA analysis. (G) The heatmap reflects the changes in key pathways in different T-cell subsets. The pathways of significant upregulation (H) and significant downregulation (I) of NK cells in GSVA analysis. (J) The heatmap reflects the changes in key pathways in different NK cell subsets. CTL, cytotoxic T lymphocyte; GSVA, Gene Set Variation Analysis; NK, natural killer; Treg, regulatory T cell; UMAP, Uniform Manifold Approximation and Projection.

antiviral-like and chemotactic responses, likely triggered by DAMPs released post-IRE. Conversely, pathways regulating NK-T-cell differentiation, $CD8^+$ T-cell activation, macrophage differentiation, and negative regulation of JAK-STAT signaling were downregulated, suggesting that early after IRE, NK cells primarily assume antiviral and proinflammatory effector roles. Although overall trends were consistent across patients, IL-27-related and MCP-1-related pathways were predominantly activated in patient P4 (online supplemental Figure S6 and S7), reflecting interindividual variability. Subtype analysis revealed that CD56dim NK cells upregulated "antiviral innate immune response" and "negative regulation of viral genome replication" while downregulating inhibitory JAK-STAT regulatory pathways, indicating enhanced cytokine responsiveness (figure 3J, online supplemental Figure S8A–D). In CD56bright NK cells, GSVA scores decreased for several GO pathways related to regulation of $CD8^+$ αβ T-cell activation, regulatory T-cell differentiation, and T-cell apoptotic processes (figure 3J, online supplemental Figure S8E–H). Because these pathway names include both positive and negative regulatory processes, we interpreted these changes conservatively as evidence of altered NK-T-cell immunoregulatory signaling rather than inferring a single directional functional effect. Collectively, NK cells shift from an immunomodulatory to an antiviral effector phenotype, reflecting immune transition from acute activation toward steady-state recovery after IRE.

### Immune clonal remodeling following IRE treatment

Significant clonal expansion was observed within the T-cell compartment, particularly in specific clonotypes (figure 4A). Post-IRE, overall clonal richness (Chao1, ACE) and diversity (inverse Simpson, normalized entropy) increased (figure 4B), while abundance density curves remained similar, indicating stable global repertoire structure with selective redistribution of clonotypes across abundance classes in peripheral blood (figure 4C). Because these data derive from PBMCs, this pattern reflects circulation-level repertoire remodeling and should not be interpreted as spatial redistribution within the prostate or TME. CDR3 length distributions were largely conserved, with minor pretreatment enrichment near 15 and 27 amino acids (aa) (figure 4D). The unique clone ratio (~60%) remained unchanged (figure 4E). Clonal abundance analysis showed an increase in medium-abundance clones (10,001–30,000) and a decrease in high-abundance clones (>30,000) after treatment (figure 4F). Rarefaction and coverage analyses confirmed directed amplification of specific clones (figure 4G–I). The proportions of top 10 and top 100 high-frequency clones also increased post-IRE (figure 4J), supporting that repertoire remodeling is not driven by a single outlier. UMAP visualization revealed rare clones distributed across all subsets, enriched in $CD4^+$ central memory (CM) T cells, while small-to-medium clones were concentrated in $CD8^+$ CTL, $CD8^+$ EM, and $CD4^+$ CTL populations (figure 4K,L). Collectively, IRE enhances TCR repertoire diversity while promoting selective expansion of antigen-specific clonotypes, indicating peripheral immune repertoire remodeling after treatment.

### Rewiring of T/NK cell communication networks following IRE treatment

The overall intercellular communication among T/NK cells slightly decreased after IRE (figure 5A and D), while communication strength was redistributed in a subset-specific manner across circulating T/NK subtypes.

Because CellChat inference is based on circulating PBMC transcriptomes, these changes represent subset-level shifts in signaling potential rather than spatially localized remodeling within tissue. $CD8^+$ and $CD4^+$ CTLs exhibited stronger incoming and outgoing signals, whereas Tregs showed reduced communication (figure 5B, C and E).

Pathways related to antigen-specific activation (CD40, MHC-I), migration and adhesion (ITGB2, ADGRE5), and systemic inflammation (MIF) were broadly downregulated, indicating reduced antigen-presentation-associated signaling and a shift from an aggressive to a balanced immune state. Conversely, BAG6 and CD48 signaling were enhanced, reflecting a transition from adaptive hyperactivation to innate surveillance (figure 5F). Decreased MHC-I and MIF signaling was observed across multiple subsets, including $CD8^+$ EM T, $CD56^+$dim NK, $CD8^+$ CTL, $CD56^+$bright NK, $CD8^+$ naïve, and MAIT cells, suggesting immune reconstitution toward homeostasis (figure 5G). Ligand-receptor interaction maps illustrate these network-level shifts (figure 5H,I).

For key subsets ($CD8^+$ CTL, $CD4^+$ CTL, $CD8^+$ EM T, $CD56^+$dim NK, and Tregs), TF analysis revealed substantial regulatory remodeling. RSS plots identified subset-specific regulons, and violin plots highlighted the 12 most altered TFs (online supplemental Figure S9–S13). Notably, ETS1, TBX21, RUNX3, IRF1, and IKZF1 were upregulated across multiple populations, indicating that IRE enhances effector differentiation and immune activation programs in T/NK cells (figure 5J).

### Broadly activated myeloid cell-mediated antigen presentation and antiviral response

Myeloid cells were classified into classical and non-classical monocytes, neutrophils, megakaryocytes, and DCs based on marker expression (figure 6A,B and E). Although PBMCs typically lack neutrophils, a small fraction was detected due to sample handling. Classical monocytes were predominant, while non-classical monocytes increased after IRE (figure 6C,D).

Post-IRE, myeloid cells exhibited marked activation, with upregulated pathways related to antiviral response, antigen presentation, complement

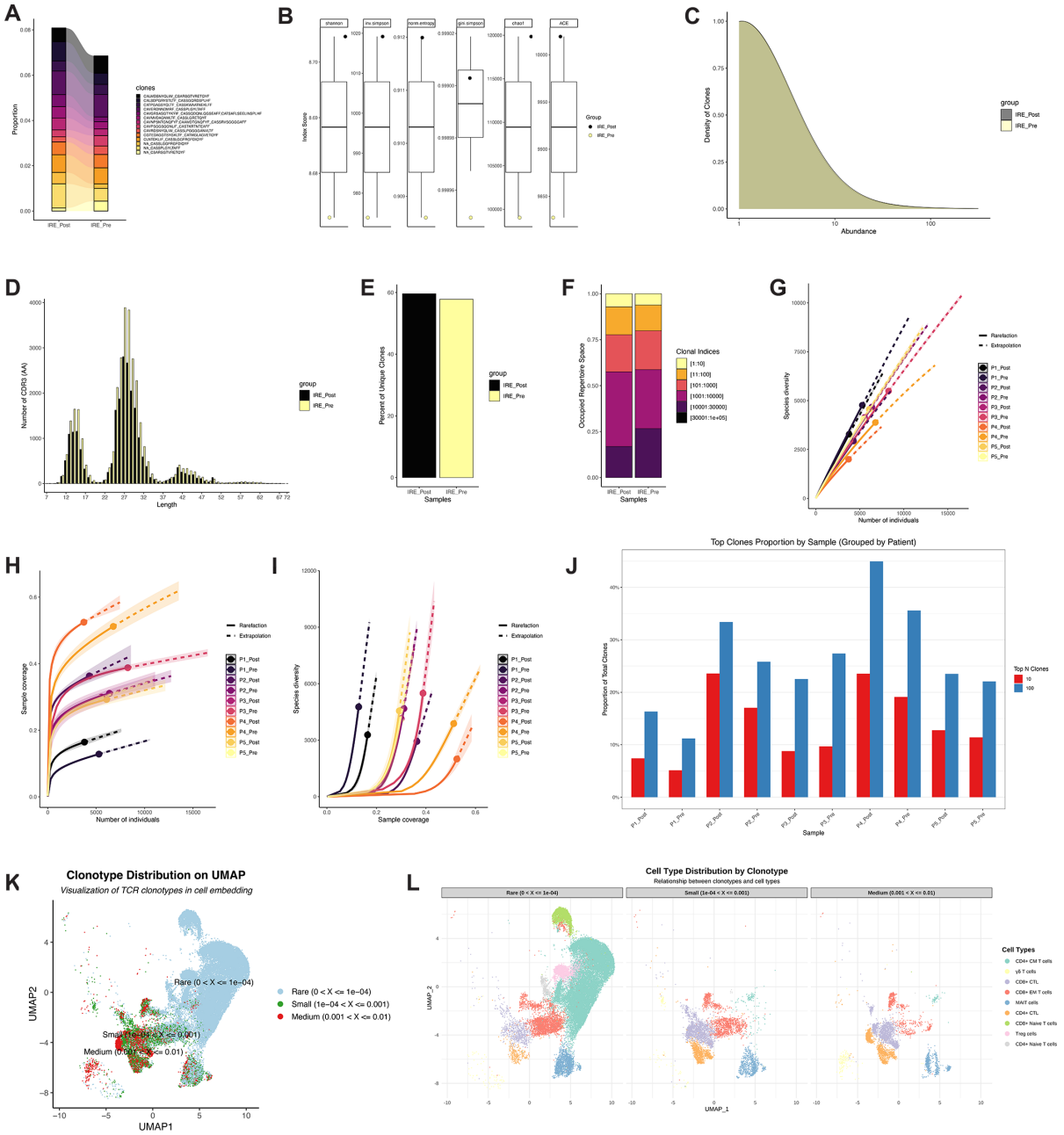


**Figure 4** TCR repertoire remodeling in PBMC T cells before and after IRE. (A) Stacked bar plot showing the relative proportions of the most abundant clonotypes in the pre-IRE and post-IRE groups, highlighting dominant expanded clones. (B) Comparison of clonal richness and diversity indices between pretreatment and post-treatment samples, indicating a global increase in both richness and diversity after IRE. (C) Overlaid abundance density distributions of clonotype frequencies for the pre-IRE and post-IRE groups; the two density curves are highly similar and therefore largely overlap (appearing as a single curve). (D) CDR3 length distribution of TCRs. (E) Unique clonotype proportion across pretreatment and post-treatment samples. (F) Composition of clonotypes across different abundance intervals, illustrating the relative proportion of low-frequency, medium-frequency, and high-frequency clones. (G) Rarefaction curves showing clonotype richness as a function of sampling depth in pretreatment and post-treatment repertoires. (H–I) Rarefaction and coverage analyses comparing repertoire completeness and saturation between groups. (J) Fraction of the top 10 and top 100 high-frequency clones within each patient, indicating dominance of expanded clonotypes. (K–L) UMAP visualization showing the distribution of TCR clonotypes with different abundance levels across major T-cell subsets. IRE, irreversible electroporation; NK, natural killer; PBMC, peripheral blood mononuclear cell; TCR, T-cell receptor; UMAP, Uniform Manifold Approximation and Projection.

activation, cytokine secretion, and interferon signaling, indicating transition from quiescence to an immune-reactive state (figure 6F, online supplemental Figure S14–S16). Functional heatmaps showed pronounced activation of inflammatory and complement pathways in non-classical and classical monocytes, whereas lipid metabolism, angiogenesis, and stress-sensing pathways were downregulated

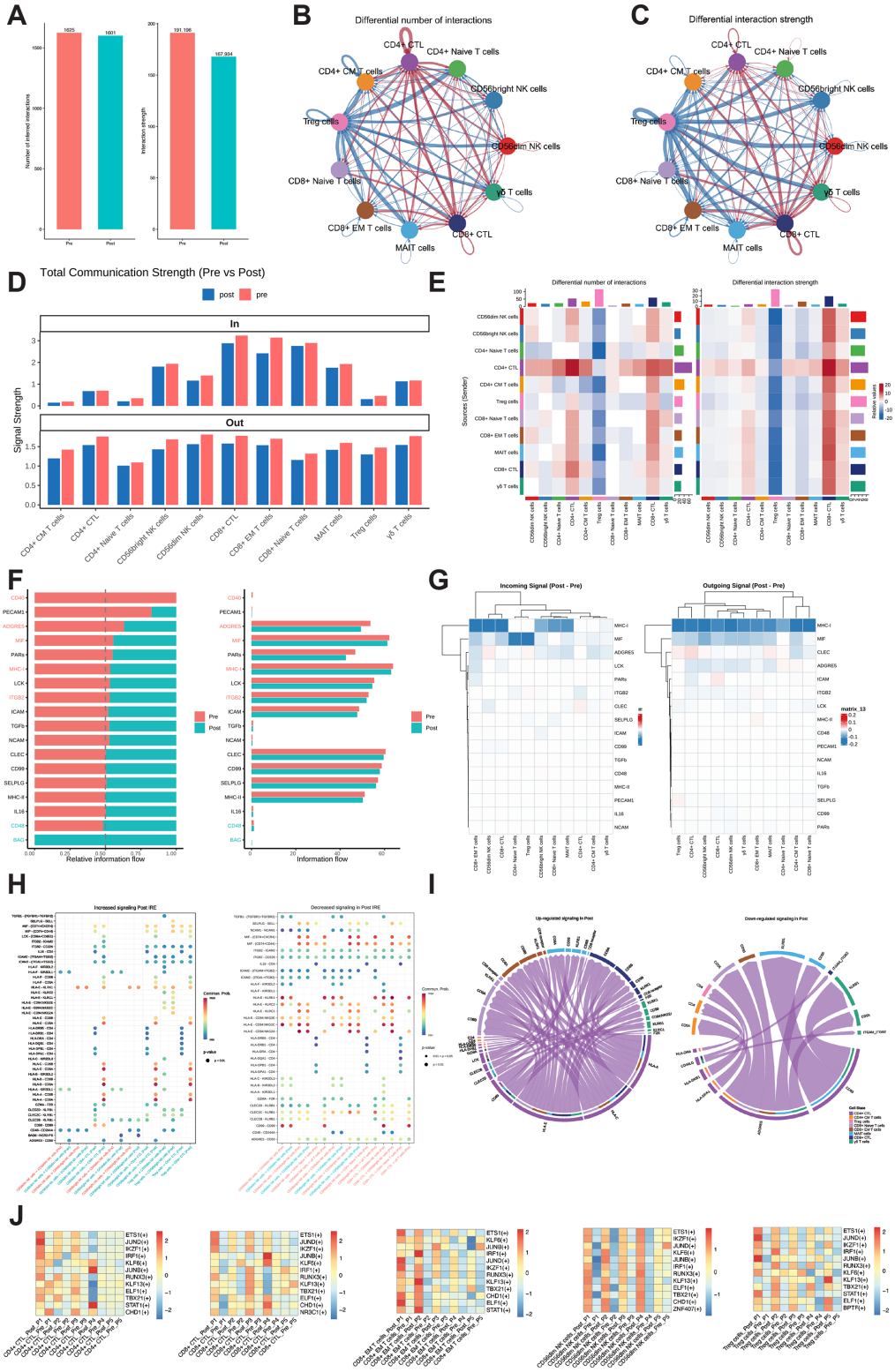


**Figure 5** (A) Global quantification of intercellular communication probability among T/NK cells before and after IRE treatment. (B–C) Network visualization of signal interaction number and strength across major T/NK subsets, illustrating treatment-induced redistribution of communication activity. (D) Overall comparison of total communication strength between groups in different cell groups. (E) Heatmap showing changes in outgoing and incoming signaling strength (post–pre) across major T/NK subsets. (F) Relative information flow analysis summarizing global alterations in signaling pathways, highlighting pathways with increased or decreased activity after treatment. (G) Quantitative heatmap displaying pathway-specific differences in outgoing and incoming signaling among distinct T/NK cell subsets. (H–I) Bubble and chord plots illustrating differential ligand-receptor interactions between representative T/NK subsets before and after IRE treatment. (J) Transcription factor regulatory analysis of key T/NK subsets, including CD8$^+$ CTL, CD4$^+$ CTL, CD8$^+$ EM T, CD56 dim NK, and Treg cells. CM, central memory; CTL, cytotoxic T lymphocyte; EM, effector memory; IRE, irreversible electroporation; NK, natural killer; Treg, regulatory T cell.

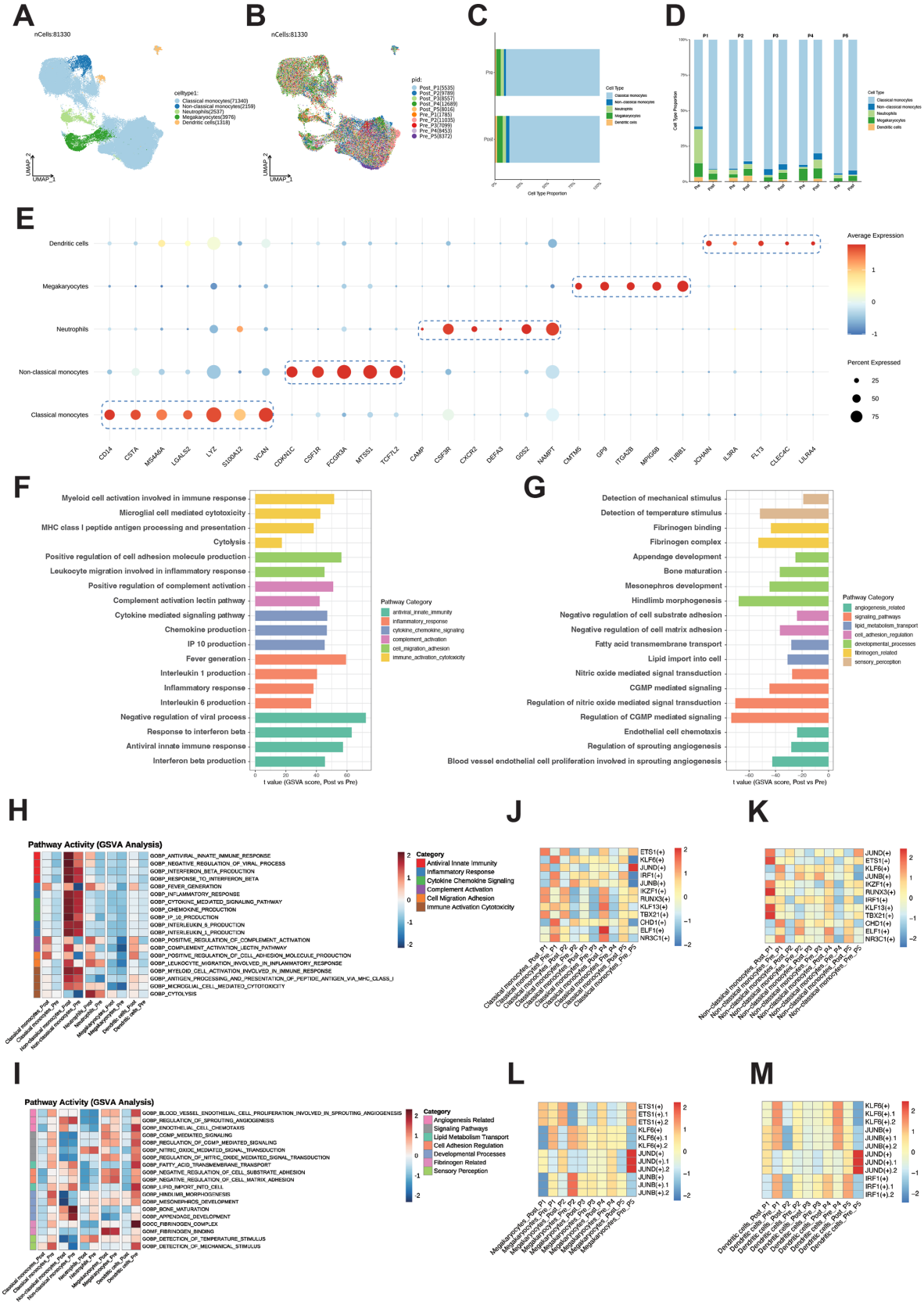


**Figure 6** (A) The UMAP dimensionality reduction results of myeloid cell subtypes. (B) The UMAP dimensionality reduction results of different patients. The overall proportion of various myeloid cell subtypes (C) and their proportions in each patient (D). (E) The expression of various myeloid cells for their specific markers. The pathways of significant upregulation (F) and significant downregulation (G) of T cells in GSVA analysis. The heatmap reflects the changes in upregulated (H) and downregulated (I) pathways in different T-cell subsets. (J–M) Transcription factor regulatory analysis of key myeloid subsets. GSVA, Gene Set Variation Analysis; UMAP, Uniform Manifold Approximation and Projection.

(figure 6G–I). These findings suggest IRE elicits systemic innate immune activation while transiently suppressing homeostatic and metabolic functions.

TF analysis revealed upregulation of IKZF1, RUNX3, KLF13, and TBX21 in monocytes, reflecting coordinated immune remodeling toward type I immunity and interferon-driven activation (figure 6J,K, online supplemental Figure S17 and S18). Although megakaryocytes and DCs were less abundant, their profiles showed heterogeneous regulation (figure 6L,M, online supplemental Figure S19 and S20). Collectively, IRE reprograms myeloid cells toward an "activated yet controlled" phenotype, balancing proinflammatory activation with mechanisms of immune restraint.

### Rewiring of intracellular communication patterns in myeloid cells

Following IRE, myeloid cells exhibited an overall increase in intercellular interaction number but reduced interaction strength (figure 7A,D). Non-classical monocytes showed expanded outgoing signaling despite diminished signal intensity, while DCs displayed increased bidirectional communication with classical monocytes (figure 7B–E). Pathways involving ITGB2, SELPLG, ICAM, APP, ESAM, TNF, and RESISTIN were upregulated, indicating enhanced immune cell adhesion, migration, and inflammation. Conversely, VISFATIN, CLEC, MIF, ADGRE5, and ANNEXIN pathways were downregulated, reflecting dampened immunosuppressive signaling (figure 7F). Key amplified axes included TNF–TNFRSF1B, SELPLG–SELL, ICAM–ITGB2, RETN–CAP1, and PECAM1–PECAM1, whereas suppressive interactions such as MIF–CD74/CXCR4, LGALS9–CD45/CD44, ANXA1–FPR1, and ADGRE5–CD55 declined (figure 7G,H). Collectively, these results suggest that IRE enhances myeloid-driven inflammatory communication while attenuating inhibitory immune signaling.

### B-cell functional conversion characterized by enhanced inflammation sensing and concurrent metabolic dysfunction

B cells were categorized into memory, naïve, transitional, plasma, and activated subtypes based on canonical marker expression (figure 8A,D). Cellular composition varied across patients, with memory B cells showing a general post-IRE increase (figure 8B,C). Functionally, IRE-induced tissue necrosis and DAMPs release activated TLR4, complement, and acute-phase response pathways, indicating enhanced innate signaling (figure 8E, online supplemental Figure S21). Meanwhile, metabolic suppression, ROS accumulation, and hypoxia impaired energy metabolism and MHC-II antigen presentation, reflecting a shift from adaptive effector to metabolically restrained inflammatory states (figure 8F, online supplemental Figure S21). These patterns were largely consistent among patients, though P4 exhibited stronger activation (online supplemental Figure S22 and S23). Pathway enrichment revealed pronounced activation of innate immune, extracellular matrix adhesion, proteolysis, and autocrine signaling pathways—particularly in memory B cells—accompanied by downregulation of cell cycle and metabolic programs (figure 8G). TF analysis showed no major pretreatment versus post-treatment differences (figure 8H–J, online supplemental Figure S24 and S25). Collectively, IRE induces functional reprogramming of B cells toward innate-like activation, with memory B cells showing the most prominent remodeling.

### IRE reshapes the holistic cellular communication pattern in PBMCs

Figure 9A shows the UMAP distribution of all immune subpopulations. Overall, the number of intercellular communications increased after IRE, while signal intensity declined (figure 9B,C). Notably, interactions from non-classical monocytes to NK and T cells, and from DCs to NK, $CD8^+$ CTL, and $CD8^+$ naïve T cells, were enhanced, whereas $CD8^+$ EM T cells exhibited the greatest reduction in received signals (figure 9D).

The PBMC communication network underwent bidirectional remodeling post-IRE: pathways such as GALECTIN, ESAM, CD6, ALCAM, TNF, and RESISTIN were upregulated, indicating strengthened inflammatory and adhesion signaling; in contrast, CD40, CD86, ADGRE5, PECAM1, THBS, SEMA4, MHC-I, and VISFATIN were downregulated, reflecting attenuated antigen presentation and costimulatory signaling (figure 9E,F). These findings suggest a rebalanced immune landscape characterized by enhanced inflammatory communication and reduced antigen-specific activation. Ligand-receptor interaction maps before and after treatment further visualize these changes (figure 9G,H).

### Checkpoint-related receptor and ligand expression in peripheral T/NK and myeloid compartments after IRE

We additionally profiled immune checkpoint-related receptor and ligand/costimulatory gene expression across peripheral immune subsets in our paired pre-IRE/post-IRE PBMC scRNA-seq dataset (online supplemental Figure S27). DotPlot visualization (dot size, fraction of expressing cells; dot color, average expression) revealed pronounced subset-specific patterns rather than uniform checkpoint upregulation across circulating lymphocytes.

Within the T/NK compartment, Treg cells displayed the most prominent expression of canonical inhibitory markers (CTLA4, TIGIT, and TOX), whereas NK-cell, γδ T-cell, and MAIT-cell subsets preferentially expressed innate/NK-associated inhibitory receptors (notably KLRC1 and CD96). In contrast, PDCD1 and HAVCR2 were generally low across most circulating T-cell subsets at postoperative day 7. Summarizing within-subset changes (log2 fold change, post vs pre) suggested overall modest shifts with cell-type-dependent remodeling, including subset-divergent changes in KLRC1 and increased LILRB1/LILRB2 signatures in selected effector-like T-cell subsets.

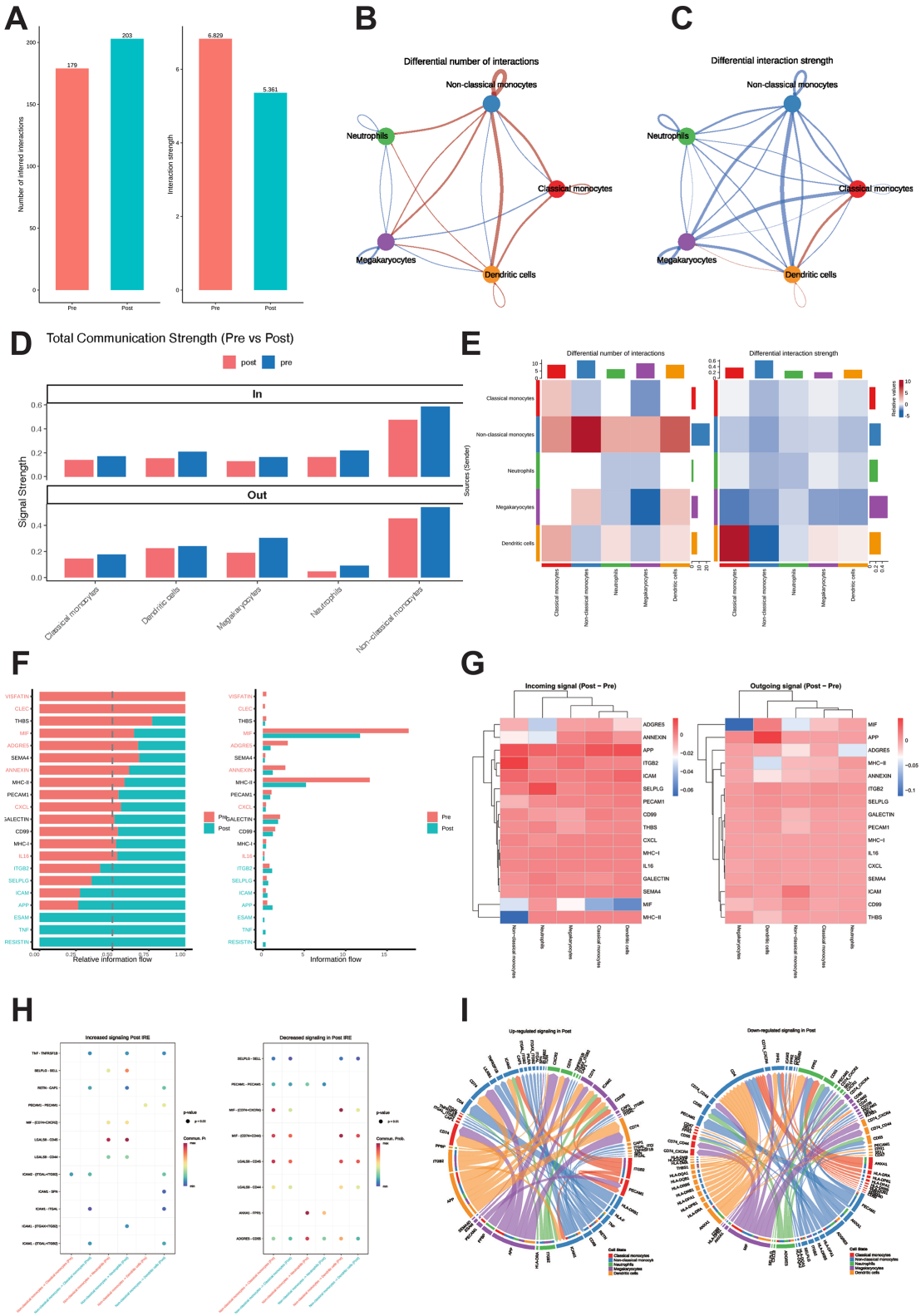


**Figure 7** (A) Global quantification of intercellular communication probability among myeloid cells before and after IRE treatment. (B–C) Network visualization of signal interaction number and strength across major myeloid subsets, illustrating treatment-induced redistribution of communication activity. (D) Overall comparison of total communication strength between groups in different cell groups. (E) Heatmap showing changes in outgoing and incoming signaling strength (post–pre) across major myeloid subsets. (F) Relative information flow analysis summarizing global alterations in signaling pathways, highlighting pathways with increased or decreased activity after treatment. (G) Quantitative heatmap displaying pathway-specific differences in outgoing and incoming signaling among distinct myeloid cells subsets. (H–I) Bubble and chord plots illustrating differential ligand-receptor interactions between representative myeloid cells subsets before and after IRE treatment. IRE, irreversible electroporation.

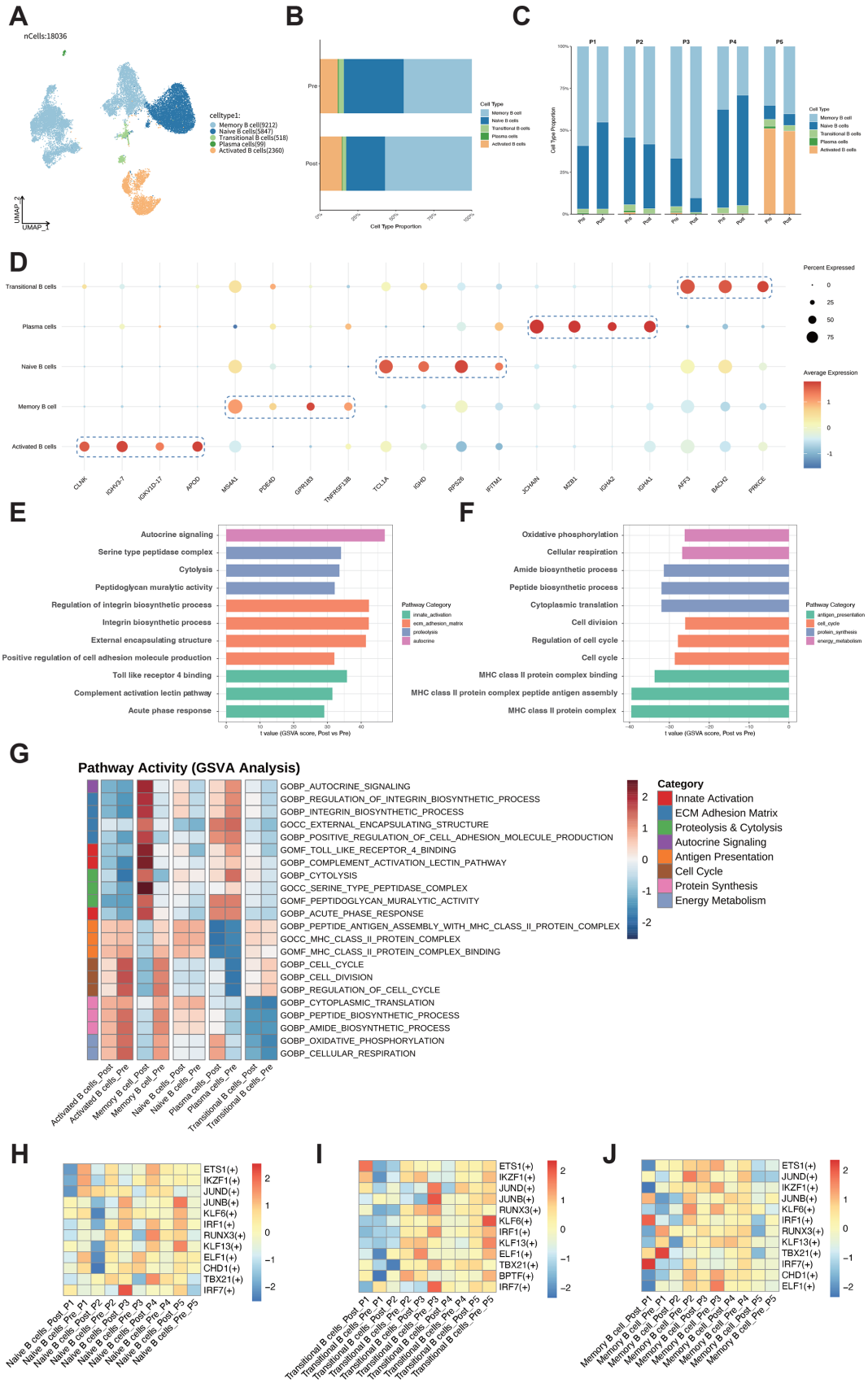


**Figure 8** (A) The UMAP dimensionality reduction results of B-cell subtypes. The overall proportion of various B-cell subtypes (B) and their proportions in each patient (C). (D) The expression of various B cells for their specific markers. The pathways of significant upregulation (E) and significant downregulation (F) of B cells in GSVA analysis. (G) The heatmap reflects the changes in key pathways in different B-cell subsets. (H–J) The heatmap reflects the changes in key pathways in different B-cell subsets. GSVA, Gene Set Variation Analysis; UMAP, Uniform Manifold Approximation and Projection.

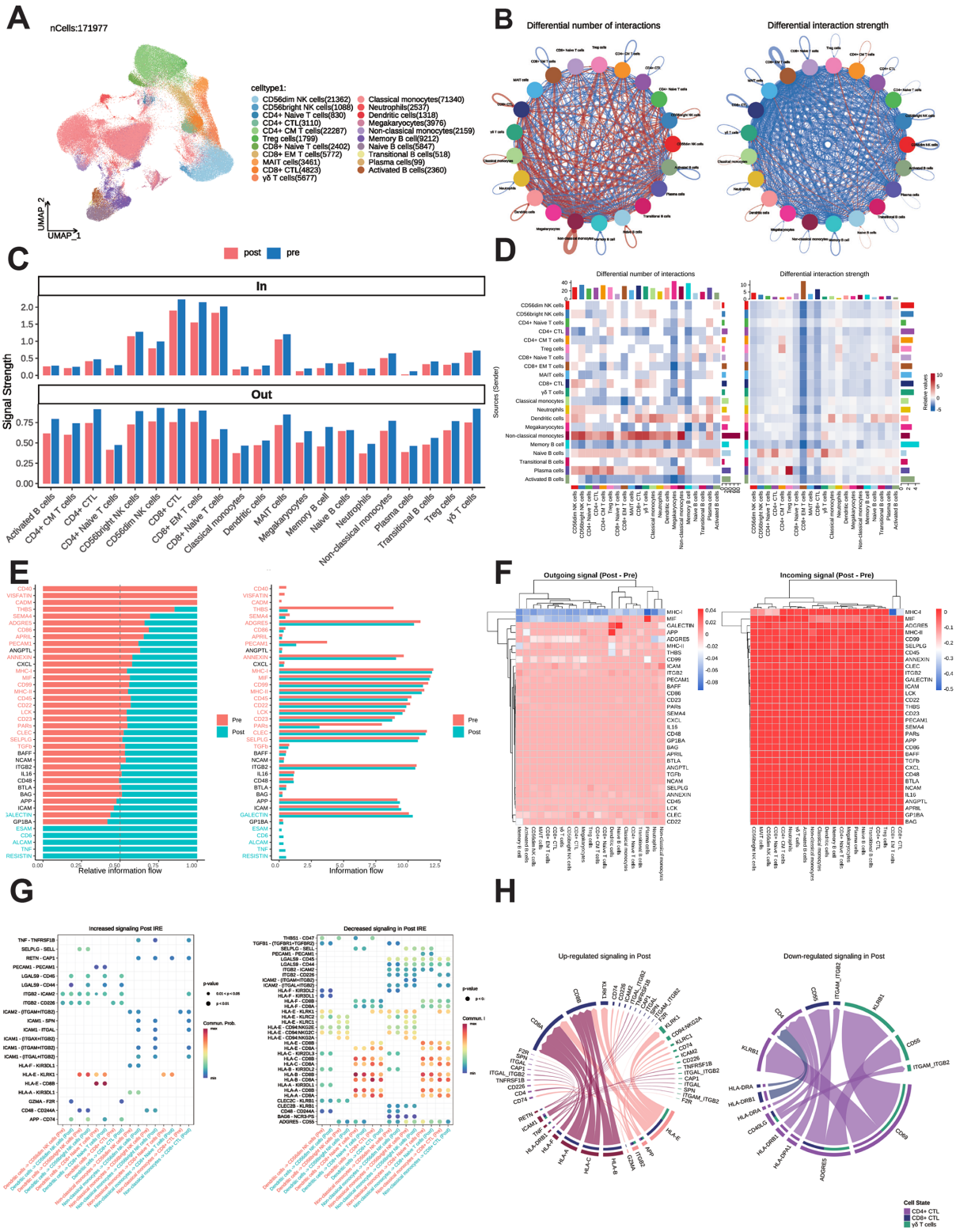


**Figure 9** (A) UMAP dimension reduction for whole-cell subtypes. (B) Network visualization of signal interaction number and strength across all cell subtypes. (C) Overall comparison of total communication strength between groups in different cell groups. (D) Heatmap showing changes in outgoing and incoming signaling strength (post–pre) across all cell subtypes. (F) Relative information flow analysis summarizing global alterations in signaling pathways, highlighting pathways with increased or decreased activity after treatment. (G) Quantitative heatmap displaying pathway-specific differences in outgoing and incoming signaling among all cell subtypes. (H–I) Bubble and chord plots illustrating differential ligand-receptor interactions between representative cells subsets before and after IRE treatment. CM, central memory; CTL, cytotoxic T lymphocyte; EM, effector memory; IRE, irreversible electroporation; NK, natural killer; UMAP, Uniform Manifold Approximation and Projection.

In the myeloid compartment, expression of checkpoint ligand/costimulatory genes (CD274/PD-L1, PDCD1LG2/PD-L2, CD80, CD86, and CD40) was low-to-moderate but subset-specific. Notably, CD274 (PD-L1) increased after IRE in multiple myeloid subsets, while PDCD1LG2 and CD80/CD86 showed divergent directions across myeloid lineages. Overall, these data indicate that at day 7 post-IRE, peripheral checkpoint landscapes undergo time-dependent and subset-dependent remodeling, with concurrent attenuation of some Treg-associated inhibitory features and emergence of a myeloid PD-L1 axis that may be relevant to rational checkpoint blockade combination strategies.

## DISCUSSION

We present the first single-cell transcriptomic and TCR repertoire profiling of peripheral immune remodeling after IRE in localized PCa. Paired pretreatment and post-treatment analyses reveal dynamic bidirectional reprogramming characterized by strong innate activation (myeloid and NK cells) and transient suppression followed by recovery of adaptive T-cell immunity. These findings demonstrate that IRE functions not only as a local ablative therapy but also as an immunomodulatory intervention reshaping systemic immune homeostasis.

Notably, this study provides the first evidence that IRE induces an interferon-driven, antiviral-like immune response in PCa. IRE enhances type I interferon signaling and ISG expression, accompanied by activation of myeloid and NK cells. Elevated non-classical monocytes and DC activity indicate rapid systemic innate activation, likely triggered by DAMP and tumor antigen release. Upregulation of RUNX3, TBX21, and IKZF1 suggests a coordinated transcriptional program promoting antigen presentation and antiviral-like defense while controlling inflammation.[22] This "activated yet regulated" phenotype resembles the transient inflammatory burst observed after immunogenic cell death, providing mechanistic evidence for IRE's proposed "in situ vaccination" effect.[23 24] Notably, we report for the first time that IRE activation induces an antitumor-like immune response following surgery. Previous study has indicated that high expression of interferon-related genes correlates positively with response to chemotherapy/radiotherapy/immune checkpoint inhibitors (ICBs).[25] Additionally, PCa, as a "cold tumor," lacks immune infiltration and exhibits poor response to ICB. Activation of interferon-related pathways can transform cold tumors into hot tumors, thereby enhancing therapeutic responsiveness.[26 27] Thus, IRE is expected to enhance the responsiveness of PCa to immunotherapy by activating antiviral-like responses in myeloid cells and NK cells, providing a theoretical basis for combination therapies.

In contrast to enhanced innate immunity, circulating T cells at day 7 exhibited downregulation of activation-associated and proliferation-associated transcriptional programs after IRE. We interpret this pattern as an early transitional state in peripheral adaptive immunity rather than definitive loss of antitumor potential. Importantly, this does not necessarily conflict with prior clinical immune-monitoring data in prostate IRE. In the IRE-IMMUNO study, Geboers *et al* used multi-time point peripheral blood analyses (days 5, 14, and 30) and reported reduced systemic immune suppression with effector T-cell activation peaking at approximately day 14, together with evidence of PCa-specific T-cell responses. Viewed together, their functional kinetics and our day 7 scRNA-seq/TCR snapshot suggest that post-IRE T-cell immunity may evolve in phases, with early peripheral immune rebalancing followed by stronger effector activation in a later window in at least a subset of patients.[14]

Concurrently, transcriptomic pathway signatures related to activation-induced cell death (AICD) and survival signaling were altered at day 7. These patterns are compatible with a transitional "functional reset"-like state rather than terminal exhaustion, but this interpretation remains inferential and should be validated by orthogonal functional assays.[28] AICD eliminates overactivated T-cell clones via Fas/FasL-mediated apoptosis; suppression of pro-apoptotic signaling or induction of survival programs may reduce AICD sensitivity and prolong viability. Sustained expression of effector TFs (RUNX3, TBX21, IRF1, ETS1), together with enhanced TCR clonal expansion, supports amplification or selective retention of antigen-specific clones post-IRE, with the observed "quiescent" state reflecting persistence rather than exhaustion.[29] This adaptive equilibrium suggests that, following innate activation and reduced tumor burden, weakened TCR/co-stimulatory signaling may favor maintenance of expanded T-cell clones as a "quiescent but reactivable" pool rather than AICD-mediated deletion. Additionally, upregulated IL-27 and interferon pathways in T and NK cells may support $CD8^+$ T-cell survival, self-renewal, and effector function.[30 31] Similar transient suppression after radiofrequency or cryoablation also supports the concept of systemic immune homeostasis recovery after local ablation.[32 33]

Beyond T and NK cells, single-cell analysis reveals dynamic remodeling of B-cell function after IRE. Memory B cells show upregulated TLR4 and complement-related inflammatory signaling but downregulated metabolic and antigen-presentation pathways (eg, MHC-II, oxidative phosphorylation). This indicates functional reprogramming within the IRE-induced inflammatory milieu, featuring "enhanced inflammatory sensing but suppressed effector function." The enrichment of memory-like B cells suggests selective retention of antigen-experienced clones, supporting postoperative humoral immune memory.[34] Given that B cells can influence T-cell responses through cytokine secretion and antigen processing, this transcriptional remodeling may facilitate

fine-tuned synergistic regulation between humoral and cellular immunity, promoting orderly recovery of systemic immunity following IRE.

Cellular communication analysis revealed a systemic reorganization of peripheral immune signaling after IRE. Proinflammatory pathways mediated by MHC-I/CD40 and MIF were markedly attenuated, whereas immune homeostasis pathways involving BAG6 and CD48 were enhanced, indicating a transition from inflammation-driven to surveillance-oriented communication. Mechanistically, this reflects an IRE-induced activation–recovery program at the systemic level. The decline in MHC-I/CD40 signaling aligns with reduced T-cell proliferation, while upregulated BAG6–NKp30 and CD48–CD2 interactions promote immune surveillance and prevent excessive inflammation.[35–37]

Overall, this study reveals that IRE is a therapeutic modality that combines localized ablation with systemic immune modulation. Its "activation-recovery" biphasic immune process provides a temporal window for subsequent combination immunotherapies (such as immune checkpoint inhibition or cytokine therapy). Peripheral immune monitoring using single-cell transcriptomics and TCR sequencing can serve as a biomarker platform for assessing immune activation dynamics and guiding personalized treatment timing. Future studies should expand sample sizes, incorporate multi-time point follow-ups, and integrate tissue-level immunomics analysis to comprehensively elucidate the spatiotemporal characteristics of immune remodeling following IRE.

This study has certain limitations. First, immune profiling was performed on peripheral blood samples collected at a single postoperative time point (day 7), which may not fully capture the temporal dynamics of immune remodeling after IRE. In particular, recent multi-time point peripheral immune monitoring after IRE in localized PCa suggests that some effector T-cell activation signals may peak later (eg, around day 14), underscoring that our day 7 sampling captures an early phase rather than the full response trajectory.[14] Second, the relatively small sample size limits the generalizability of our findings and warrants validation in larger, independent cohorts. Third, because our analyses were based on PBMCs, they primarily reflect systemic immune remodeling rather than the spatially resolved intratumoral TME. While prior studies suggest that peripheral immune dynamics can partially mirror TME-associated immune changes and may serve as a practical, non-invasive monitoring strategy,[38 39] direct linkage between circulating immune signatures and local intratumoral immune states will require future studies integrating paired tumor biopsies and/or spatial profiling across multiple post-treatment time points. Fourth, the inferred signaling pathways and cell–cell communication networks in this study were derived from transcriptomic analyses and should therefore be interpreted with caution until validated by orthogonal functional assays. Finally, we did not assess long-term clinical outcomes. Future prospective studies with paired pretreatment and post-treatment sampling, extended follow-up, and clinical outcome evaluation will be needed to define the prognostic and therapeutic relevance of these immune changes and to better inform rational combination strategies with immunotherapy.

## CONCLUSION

In summary, this study systematically revealed the remodeling characteristics of the peripheral immune system following IRE treatment in PCa through single-cell transcriptomics analysis. IRE not only rapidly activates innate immunity but also induces coordinated functional reprogramming of adaptive immune cells, accompanied by systemic reorganization of cytokine signaling regulation and intercellular communication networks. Notably, the activation of interferon-related pathways and enhanced immune signaling exchange suggest that IRE may drive PCa from an immune "cold tumor" to a "responding" state. Overall, IRE exhibits dual effects of local ablation and systemic immune modulation, providing crucial mechanistic evidence and theoretical foundations for its combined application with immunotherapy.

**Acknowledgements** We thank OE Biotech Co., Ltd. (Shanghai, China) for technical support in sequencing.

**Contributors** Study Concept and Design: JCX, ZYX, SGW, QDX contributed to the conception and design of the study. Data Acquisition: JY, JCX, JXS contributed to the acquisition of data. Data Analysis and Interpretation: JCX, ZYX, GCY performed the statistical analysis. Data Collation: JCX, ZYX collated the raw results. Data Visualization: JCX, QDX visualized the data. Draft Writing: JCX, ZYX wrote the first draft of the manuscript. Manuscript Revision: SGW, QDX, JY, JCX, YW revised the manuscript. Equal Contribution: JCX, ZYX, JY, SGW, QDX contributed equally to this work. QDX is the guarantor of the study.

**Funding** This work was supported by the Hubei Provincial Natural Science Foundation (Youth Fund, Category B; grant No. JCZRQNB202600457).

**Competing interests** No, there are no competing interests.

**Patient consent for publication** Not applicable.

**Ethics approval** The study was approved by the Tongji Hospital Ethics Committee (Approval No.: TJ-IRB202409097). Participants gave informed consent to participate in the study before taking part.

**Provenance and peer review** Not commissioned; externally peer reviewed.

**Data availability statement** Data are available upon reasonable request. The single-cell RNA sequencing data generated in this study have been deposited in the National Genomics Data Center (NGDC) under accession number PRJCA046947 and are currently pending public release. The data will be made publicly available upon release by the repository. Until then, relevant data are available from the corresponding author upon reasonable request.

**ORCID iDs**
Shao-Gang Wang https://orcid.org/0000-0002-3206-1495
Qi-Dong Xia https://orcid.org/0000-0002-2278-1122

## REFERENCES

1 Siegel RL, Kratzer TB, Giaquinto AN, *et al*. Cancer statistics, 2025. *CA Cancer J Clin* 2025;75:10–45.
2 Wong MCS, Goggins WB, Wang HHX, *et al*. Global Incidence and Mortality for Prostate Cancer: Analysis of Temporal Patterns and Trends in 36 Countries. *Eur Urol* 2016;70:862–74.
3 Cornford P, van den Bergh RCN, Briers E, *et al*. EAU-EANM-ESTRO-ESUR-ISUP-SIOG Guidelines on Prostate Cancer-2024 Update. Part I: Screening, Diagnosis, and Local Treatment with Curative Intent. *Eur Urol* 2024;86:148–63.
4 Al Hussein Al Awamlh B, Wallis CJD, Penson DF, *et al*. Functional Outcomes After Localized Prostate Cancer Treatment. *JAMA* 2024;331:302.
5 Feng D, Li D, Xiao Y, *et al*. Focal ablation therapy presents promising results for selectively localized prostate cancer patients. *Chinese Journal of Cancer Research* 2023;35:424–30.
6 Valerio M, Cerantola Y, Eggener SE, *et al*. New and Established Technology in Focal Ablation of the Prostate: A Systematic Review. *Eur Urol* 2017;71:17–34.
7 Blazevski A, Scheltema MJ, Amin A, *et al*. Irreversible electroporation (IRE): a narrative review of the development of IRE from the laboratory to a prostate cancer treatment. *BJU Int* 2020;125:369–78.
8 Faiella E, Santucci D, Vertulli D, *et al*. Irreversible Electroporation (IRE) for Prostate Cancer (PCa) Treatment: The State of the Art. *J Pers Med* 2024;14:137.
9 Arena CB, Sano MB, Rossmeisl JH Jr, *et al*. High-frequency irreversible electroporation (H-FIRE) for non-thermal ablation without muscle contraction. *Biomed Eng Online* 2011;10:102.
10 He C, Huang X, Zhang Y, *et al*. T-cell activation and immune memory enhancement induced by irreversible electroporation in pancreatic cancer. *Clin Transl Med* 2020;10:e39.
11 Bertheloot D, Latz E, Franklin BS. Necroptosis, pyroptosis and apoptosis: an intricate game of cell death. *Cell Mol Immunol* 2021;18:1106–21.
12 Dai Z, Wang Z, Lei K, *et al*. Irreversible electroporation induces CD8+ T cell immune response against post-ablation hepatocellular carcinoma growth. *Cancer Lett* 2021;503:1–10.
13 Ngwa W, Irabor OC, Schoenfeld JD, *et al*. Using immunotherapy to boost the abscopal effect. *Nat Rev Cancer* 2018;18:313–22.
14 Geboers B, Scheltema MJ, Jung J, *et al*. Irreversible electroporation of localised prostate cancer downregulates immune suppression and induces systemic anti-tumour T-cell activation - IRE-IMMUNO study. *BJU Int* 2025;135:319–28.
15 Zhang Y, Wang D, Peng M, *et al*. Single-cell RNA sequencing in cancer research. *J Exp Clin Cancer Res* 2021;40.
16 Ziegenhain C, Vieth B, Parekh S, *et al*. Comparative Analysis of Single-Cell RNA Sequencing Methods. *Mol Cell* 2017;65:631–43.
17 Hao Y, Hao S, Andersen-Nissen E, *et al*. Integrated analysis of multimodal single-cell data. *Cell* 2021;184:3573–87.
18 Quan F, Liang X, Cheng M, *et al*. Annotation of cell types (ACT): a convenient web server for cell type annotation. *Genome Med* 2023;15:91.
19 Yang L, Ng YE, Sun H, *et al*. Single-cell Mayo Map (scMayoMap): an easy-to-use tool for cell type annotation in single-cell RNA-sequencing data analysis. *BMC Biol* 2023;21:223.
20 Hänzelmann S, Castelo R, Guinney J. GSVA: gene set variation analysis for microarray and RNA-seq data. *BMC Bioinformatics* 2013;14:7.
21 Aibar S, González-Blas CB, Moerman T, *et al*. SCENIC: single-cell regulatory network inference and clustering. *Nat Methods* 2017;14:1083–6.
22 Dybska E, Adams AT, Duclaux-Loras R, *et al*. Waiting in the wings: RUNX3 reveals hidden depths of immune regulation with potential implications for inflammatory bowel disease. *Scand J Immunol* 2021;93:e13025.
23 Chikovani T, Magen E. In Situ Vaccination by Tumor Ablation: Principles and Prospects for Systemic Antitumor Immunity. *Vaccines (Basel)* 2025;13:1114.
24 Burbach BJ, O'Flanagan SD, Shao Q, *et al*. Irreversible electroporation augments checkpoint immunotherapy in prostate cancer and promotes tumor antigen-specific tissue-resident memory CD8+ T cells. *Nat Commun* 2021;12:3862.
25 Brockwell NK, Rautela J, Owen KL, *et al*. Tumor inherent interferon regulators as biomarkers of long-term chemotherapeutic response in TNBC. *NPJ Precis Oncol* 2019;3:21.
26 Vitiello GAF, Ferreira WAS, Cordeiro de Lima VC, *et al*. Antiviral Responses in Cancer: Boosting Antitumor Immunity Through Activation of Interferon Pathway in the Tumor Microenvironment. *Front Immunol* 2021;12:782852.
27 Xia Z-Y, Xiang J-C, Xu J-Z, *et al*. Irreversible electroporation synergizes with oncolytic virus enhances the infiltration of cytotoxic T lymphocytes in the tumor immune microenvironment: a leap from focal therapy to immunotherapy for prostate cancer. *J Immunother Cancer* 2025;13:e009794.
28 Blank CU, Haining WN, Held W, *et al*. Defining "T cell exhaustion". *Nat Rev Immunol* 2019;19:665–74.
29 Fonseca R, Burn TN, Gandolfo LC, *et al*. Runx3 drives a CD8+ T cell tissue residency program that is absent in CD4+ T cells. *Nat Immunol* 2022;23:1236–45.
30 Huang Z, Zak J, Pratumchai I, *et al*. IL-27 promotes the expansion of self-renewing CD8$^+$ T cells in persistent viral infection. *J Exp Med* 2019;216:1791–808.
31 Phan AT, Aunins E, Cruz-Morales E, *et al*. The type I IFN-IL-27 axis promotes mRNA vaccine-induced CD8+T cell responses. *bioRxiv* 2025.
32 Yang L, Wei S, Liu Z, *et al*. Radiofrequency Ablation and Immunotherapy: Orchestrating the Immune Microenvironment for Improved Hepatocellular Carcinoma Control. *Immunology* 2025;176:322–36.
33 Zhang K, liu M, Cong L, *et al*. A Comparative Study of Antitumor Immunity Induced by Radiofrequency Microwave and Cryoablation in Hepatocellular Carcinoma. *Appl Biochem Biotechnol* 2024;196:4088–104.
34 Phad GE, Pinto D, Foglierini M, *et al*. Clonal structure, stability and dynamics of human memory B cells and circulating plasmablasts. *Nat Immunol* 2022;23:1076–85.
35 Agudo J, Miao Y. Stemness in solid malignancies: coping with immune attack. *Nat Rev Cancer* 2025;25:27–40.
36 Reiners KS, Topolar D, Henke A, *et al*. Soluble ligands for NK cell receptors promote evasion of chronic lymphocytic leukemia cells from NK cell anti-tumor activity. *Blood* 2013;121:3658–65.
37 Li B, Lu Y, Zhong M-C, *et al*. Cis interactions between CD2 and its ligands on T cells are required for T cell activation. *Sci Immunol* 2022;7:eabn6373.
38 Hwang M, Canzoniero JV, Rosner S, *et al*. Peripheral blood immune cell dynamics reflect antitumor immune responses and predict clinical response to immunotherapy. *J Immunother Cancer* 2022;10:e004688.
39 Griffiths JI, Wallet P, Pflieger LT, *et al*. Circulating immune cell phenotype dynamics reflect the strength of tumor-immune cell interactions in patients during immunotherapy. *Proc Natl Acad Sci U S A* 2020;117:16072–82.